Available online at www.sciencedirect.com

ScienceDirect

journal homepage: www.elsevier.com/locate/he

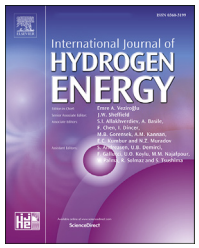

Tubular PEM electrolysis cells with a 3D-printed oxygen electrode and ALD catalyst coating

A. Laube [a,b,*], B. Sánchez Batalla [c,d], C. Weidlich [c], A. Hofer [d], J. Bachmann [d], S. Zallmann [d], C. Körner [d], S. Fischer [e], A. Chica [b], T. Struckmann [a]

[a] Hamburg University of Applied Sciences, Department of Mechanical Engineering and Production Management, Berliner Tor 21, 20099 Hamburg, Germany

[b] Instituto de Tecnología Química, Universitat Politècnica de València - Consejo Superior de Investigaciones Científicas, Avenida de Los Naranjos s/n, 46022 Valencia, Spain

[c] DECHEMA Forschungsinstitut, Applied Electrochemistry, Theodor-Heuss-Allee 25, 60486 Frankfurt am Main, Germany

[d] Friedrich-Alexander Universität Erlangen-Nuernberg, Chemistry of Thin Film Materials (CTFM), IZNF, Cauerstr. 3, 91058 Erlangen, Germany

[e] UNIWELL Rohrsysteme GmbH, Siegelfelder Straße 1, 96106 Ebern, Germany

HIGHLIGHTS

- Improved tubular PEM electrolysis cell design.
- Implementation of additive manufactured titanium porous transport electrodes.
- Utilisation of porous transport electrodes with low catalyst loading by atom layer deposition.
- Experimental characterisation of a tubular PEM electrolysis cell with pH-study.

ARTICLE INFO

Article history:
Received 20 March 2023
Received in revised form
26 May 2023
Accepted 7 August 2023
Available online 29 August 2023

Keywords:
PEM water electrolysis
Cylindrical cell design
Additive manufacturing

ABSTRACT

Polymer electrolyte membrane electrolysis (PEMEL) is a technology with a major role in linking the hydrogen production to renewable energy resources with a volatile behaviour such as wind and solar. High amounts of precious metals and a labour intensive production also make it a cost intensive technology. A tubular cell design has the potential to reduce production costs by co-extrusion of cells which feature a reduced sealing length. For the inner half cell, additive manufacturing (AM) of titanium offers a high degree of freedom for the electrode design to reach a high electric conductivity and active surface area. In combination with atomic layer deposition (ALD) of iridium catalyst a porous transport electrode (PTE) can be fabricated. Using planar test cell results and model based PTE design, this study demonstrates the feasibility of a tubular PEMEL cell consisting of an additively manufactured, iridium coated anode PTE in the inner half cell, an extruded membrane and a platinum coated graphite felt cathode PTE in the outer half cell. The outer titanium current collector can be replaced by an extruded graphite polymer compound current collector to reduce the amount of titanium without performance losses. The cell is operated at 60 °C in 1 mol L^{-1} sulphuric acid and experimentally characterized by polarization curves and electrochemical impedance spectroscopy (EIS). At 2.0 V cell potential a current

* *Corresponding author*. Hamburg University of Applied Sciences, Department of Mechanical Engineering and Production Management, Berliner Tor 21, 20099, Hamburg, Germany.
E-mail address: arlau1@upv.edu.es (A. Laube).

https://doi.org/10.1016/j.ijhydene.2023.08.084

density of ≈450 mA cm^{-2} was reached corresponding to an iridium mass specific current density >1500Ag^{-1} which is significant larger than literature values.

1. Introduction

Hydrogen and its production will have a key role if energy shall be produced fully by renewable resources [1–3]. The most investigated and developed technologies to produce hydrogen from electric energy are alkaline electrolysis (AEL) and polymer electrolyte electrolysis (PEMEL). These two technologies have benefits and disadvantages concerning efficiency, system lifetime, operating conditions and costs. PEMEL combines high energy efficiency and high power density with a dynamic operation, which is important to link the hydrogen production to renewable energy resources with a volatile behaviour such as wind and solar.

Commercial PEM electrolysis cells feature a planar cell design. They usually combine titanium bipolar plates as current collectors with integrated flow channels, porous transport layers (PTL) such as graphite felts or carbon papers in the cathode half cell and titanium felts or sintered titanium substrates in the anode half cell with a catalyst coated membrane (CCM) in a stack. The cell costs of PEMEL are much higher than that of AEL since precious metal catalysts are needed for efficient cell reactions and costly current collector materials like titanium are needed due to the harsh acidic environment at the anode electrode. The main cost drivers are the platinum group metal catalysts with about 10–20%, labour costs with about 12% and the titanium bipolar plates with about 40–50% of the stack costs [4–6]. Though research on PEMEL has shown continuous progress on lowering material needs for bipolar plates and catalysts, new cell and catalyst concepts are investigated and needed to further reduce the costs [7].

A tubular cell design enables a cost efficient cell production by co-extrusion, features shorter sealing lengths and a higher stability against pressure differences between the half cells. The feasibility of tubular energy conversion cells with extruded tubular membranes and current collectors with flow fields, has already been demonstrated for all-vanadium, vanadium/air redox flow and PEM electrolysis cells [8–11].

The catalyst layers of commercial PEMEL cells with a CCM setup contain typically 0.5 – 1.0 mg cm^{-2} platinum and 1.0 – 1.5 mg cm^{-2} iridium or iridium-ruthenium (oxides) [12–15]. It is crucial to reduce the scarce iridium in catalyst loadings to meet the future global demand of hydrogen produced by electrolysis [7]. Latest research has demonstrated a reduction down to 0.2 mg cm^{-2} [16–20].

The feasibility of a PTE with a low catalyst amount applied by atomic layer deposition in a planar and tubular cell design has been demonstrated [11,21–23]. With the ALD coated PTE design, catalyst loadings of 0.08–0.12 mg cm^{-2} iridium and mass specific currents of up to 1400Ag^{-1} for planar cells and 680Ag^{-1} for tubular cells have been achieved [11,21]. In the latter study, a titanium fibre felt rolled to a tube was used as the backbone of the anode PTE in a tubular PEMEL cell. This tubular PTE featured a high active surface area but a low longitudinal electric conductivity, which resulted in a high area specific cell resistance of about 1Ωcm^2.

Additive manufacturing offers the ability to fabricate a tubular titanium PTE backbone which meets high conductivities and a large electrode surface while using low material amounts. AM of electrodes has been investigated for electrochemical flow reactors in general [24,25], but also for AEL [26–29] and tubular PEM fuel cells [30]. Agudelo et al. used AM to fabricate a tube of sintered porous material which acts as a porous transport layer and current collector in a tubular PEM fuel cell [30]. For PEMEL cells, AM by selective laser beam melting (SLM) of metal powders has been applied to fabricate bipolar plates [31], porous transport layers [33] or bipolar plates and porous transport layer combinations [32,33]. Beside to SLM, filament printing of polymers and adding a conductive metal coating [34,35] has been used to fabricate bipolar plates for PEMEL cells. All additively manufactured bipolar plates have been tested in the typical CCM setup. AM enables the realization of cell designs with few parts and thereby the reduction of contact resistances and production steps [32,33].

In this study, the feasibility and performance of a tubular PEMEL cell with an additively manufactured titanium tube as the backbone of the anode PTE with a reduced electric resistance and catalyst coating by ALD is presented. AM was used to fabricate a tubular titanium scaffold with a solid and highly conductive core structure and a sintered porous tube with a high macroscopic surface. Based on planar cell tests with two catalyst loadings and electrode thicknesses and experimentally determined material conductivities, the electrode was developed in a model based design process. The fabricated tubular electrode scaffold was anodized to create a nano structured surface featuring an increased surface area [23,36]. Iridium was applied by atomic layer deposition, to establish a fully covered anode surface with low catalyst amounts. On the cathode side, a PTE made of a graphite felt with a platinum coating by ALD was used. The electrodes are separated by an extruded tubular cation exchange membrane. While titanium outer current collectors have been used in the standard configuration, an extruded graphite compound outer current collector has been evaluated to reduce the amount of titanium.

2. Experimental

2.1. Cell design and assembly

2.1.1. Planar test cell

To investigate the effects of catalyst loading and thickness of the porous structure, the PTE design with anode electrodes

fabricated by AM was analysed in a planar test cell as described in Ref. [21]. The end plate design combines a straight parallel flow field (active cross sectional area of 5 cm^2) with electrical and hydraulic connections as well as temperature sensors in a single component.

The additively manufactured anode PTE shown in Fig. 1b is made of Titanium grade 5 and has a porous electrode cross sectional area of 5 cm^2. At one side of the porous area a solid bar with 0.5 mm width and the same thickness of the electrode and a solid flag with the dimensions 0.4 mm × 6.5 mm x 37 mm (thickness x with x length) was added in the AM process to electrically connect the electrode avoiding contact resistances to the end plate. The titanium parts where anodized and catalyst coated as described in section 2.2. Two different catalyst loadings of 100 and 200 cycles ALD and two thicknesses of 0.7 mm an 1 mm were analysed (Table 1).

The cathode PTE is realized by a thermally treated ECM 130 graphite felt with a catalyst coating of 0.28 mg cm^{-2} platinum applied by ALD. The electrodes with an uncompressed thickness of 950 μm were compressed to 500 μm.

Table 1 – Anode thickness and catalyst coating cycles of the planar test cell.

Cell ID	Thickness/mm	Catalyst coating cycles
Pl-1-1	1.0	Ir 100
Pl-2-1	1.0	Ir 200
Pl-2-0.7	0.7	Ir 200

A fumasep-F10100 membrane (Fumatech BWT) separates the anode and cathode electrodes. As shown in Fig. 1c, the cathode PTE, membrane and anode PTE are fixed by ceramic pins and flat sealing frames. The sealing frame of the cathode side is made of expanded PTFE and is thereby compressible. On the anode side the sealing frame is made of PTFE with a groove for the connection flag on the back side. To ensure a gas tight anode compartment, the groove was filled with B-46 sealant (Reltek LLC) which also fixes the position of the PTE. The compression of the cathode electrode is defined by ceramic and stainless steel spacers which are placed between the bolts as shown in Fig. 1d. While the anode PTE is electrically connected by the extending flag, the cathode PTE is connected on the back side by the end plate.

2.1.2. *Tubular test cell*

In the tubular PEM electrolysis cell a tubular membrane separates the inner from the outer half cell. As discussed in a previous publication [11], the outer half cell can be handled similar to planar cells but the tubular geometry implies constraints concerning catalyst application and electrical connection for the inner half cell. Therefore the AM anode half cell is located at the inner half cell. The arrangement of the tubular cell components is shown in Fig. 2b.

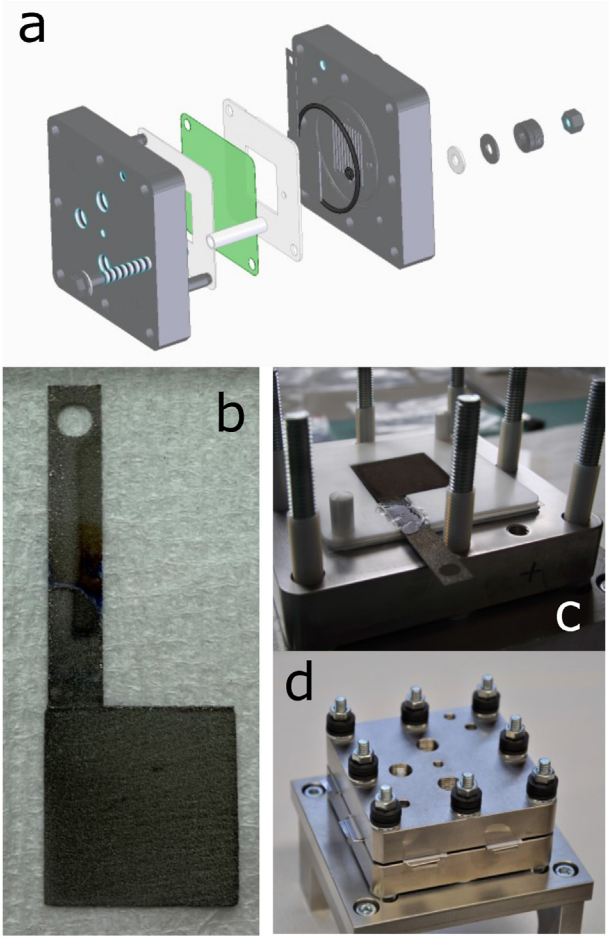

Fig. 1 – Planar test cell: (a) schematic of the cell assembly, (b) anode fabricated by AM, anodized and Ir catalyst coated by ALD, (c) stack of the planar cell components with the sealing frame of the anode electrode on top and (d) assembled planar test cell with spacers to define compression.

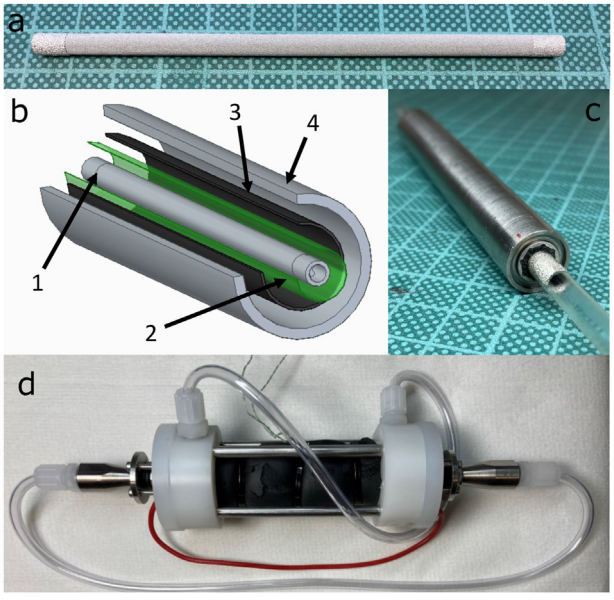

Fig. 2 – Tubular test cell: (a) tubular anode scaffold, (b) schematic of the tubular cell assembly, (c) assembled tubular test cell without and (d) with the housing for electric and hydraulic connection. In (b): (1) the tubular andode PTE, (2) extruded tubular Membrane, (3) cathode PTE and (4) Outer cathode current collector.

The anode PTE (1) is realized by an additively manufactured porous titanium tube with a solid titanium structure in the center which is connected to the tube (see Fig. 2a). The sintered tube has an outer diameter of 5 mm, a length of 108 mm and a wall thickness of 0.75 mm. The electrical resistance of three anode PTE designs was analysed by FEM calculations in Comsol 5.6 and will be described in detail in section 2.4. For the electrical connections the porous tube is extended at both ends by 7 mm long solid tubes with the same diameter and wall thickness. After the AM process, the PTE was anodized to increase the electrode surface and iridium was coated by ALD as described in section 2.2.

An extruded tubular cation exchange membrane (2) with a thickness of 100 μm separates the anode PTE from the surrounding cathode PTE (3). The membrane was extruded from membrane granulate (Fumatech BWT GmbH) used in previous studies and pretreated in separate processes as described in Refs. [10,11].

The cathode PTE, an ALD platinum coated graphite felt is realized as described above for the planar test cell. The compression from 950 μm to 500 μm is defined by the gap between the membrane and the titanium grade 2 current collector (4).

The outer current collector (Killenberg Technical Service) is 100 mm long, has an inner diameter of 6.2 mm and an outer diameter of 13 mm. Eight equally spaced, straight grooves on the circumference of the inner surface serve as parallel flow channels and two circular grooves on both ends define the compression of the external O-ring sealing. To evaluate the applicability of an extruded outer current collector, a component with comparable geometry which was extruded from graphite polymer compound and electrically connected by a copper foil as described in Ref. [10] has been used in an additional test cell.

The assembled cell is shown in Fig. 2c (without end plates) and in Fig. 2d with two identical PVDF end plates with integrated manifolds and elecrical connectors. Within the end plates, the membrane is potted into insets to seal the half cells against liquid and gas crossover. The inner half cell is electrically connected by cones which were pressed in the solid extensions of the anode PTE. To allow a liquid gas flow for the inner half cell, the connection cones are hollow and commercial tube fittings from EM-Technik were attached by a thread.

2.2. Component fabrication and characterisation

2.2.1. Scaffold fabrication

All scaffolds were produced by means of Electron Beam Powder Bed Fusion (PBF-EB) using a Q10 Plus system (ARCAM AB, GE Additive, Sweden). Gas-atomized Ti6Al4V with particle size between 45 μm and 105 μm was used. PBF-EB was performed under vacuum conditions. During PBF-EB, a thin powder layer with a defined layer thickness of 50 μm was first spread onto the build plate. The raked powder layer was then preheated using a defocused electron beam. Subsequently, the preheated layer was selectively sintered or molten according to the sliced CAD file by means of a defocused or focussed electron beam. Finally, the build plate was lowered down by the layer thickness of 50 μm. Subsequently, a new powder layer is applied [37,38].

The planar scaffolds consist of a sintered porous area and a dense molten region as a current collector. A common snake-like hatching pattern with a line offset of 200 μm was used [37,38]. After each layer, the scan pattern was rotated by 90°. Sintering was performed with a beam power of 552 W, a scan speed of 10.8 ms^{-1} and a beam focus offset at 44 mA (defocused beam); in addition, for sintering, each layer was repeatedly scanned using these process parameters for 15 times. In order to achieve a high density of the molten area, a focused electron beam was used by setting the beam focus offset at 10 mA with a beam power of 500 W and a scan velocity of 0.75 ms^{-1}. The parameters were maintained constant throughout the build process.

In similarity to the planar scaffolds, the tubular scaffolds also comprise porous and dense areas. The sintering parameters used for the porous region are identical to those used for the planar structures; while the dense areas (as current collectors) of the tubular structures were molten using a focused electron beam (beam focus offset of 10 mA) and a beam power of 201 W as well as a scan speed of 2.7 ms^{-1}.

To estimate the porosity of the porous part, planar scaffolds have been cut below the current collector and the density has been determined via weight and volume with a Kern AEJ 120-4 M scale and a calliper. With a density of 4.42 g cm^{-3} for solid titanium grade 5, the porous area has a porosity of 51%. Beside the porosity, the pore size distribution was measured with a Porolux 1000 porometer using the wetting liquid Galpore with a surface tension of 15.8 mNm^{-1}. Separate round scaffolds have been made with a circular porous area with a 16 mm diameter and a solid ring around with an outer diameter of 25 mm for sealing. Three thicknesses of 1 mm, 1.5 mm and 3 mm have been tested, but no dependency of the pore size distribution on the probe thickness could be observed. The pore size spreads between 5.5 μm and 30 μm, while 50% of the pores have a diameter between 20 μm and 30 μm.

2.2.2. Electrode preparation

The additively manufactured, tubular/planar Ti6Al4V scaffolds (anode half cell) were anodized for a duration of 4 h using 0.5 *wt*% NH_4F in a glycerol electrolyte with a water content of 12 *vol*% under an applied potential of 40 V as described in Ref. [23].

The Ir film was deposited afterwards using ALD in a commercial Gemstar-XT-6 ALD reactor from Arradiance, while the tubular electrode scaffolds were held horizontally in the chamber, hanging a few millimetres from the sample holder in order to ensure homogeneous coating all around. The samples' color turned to a homogeneous black. The nominal Ir thickness of approx. 15 nm (200 cycles) was determined on Si wafers by spectroscopic ellipsometry with a SENPro from SENTECH. Previous work has demonstrated that nucleation inhibition causes the deposit to be in particle form and the true loading in the porous titanium system to be significantly lower than this nominal value recorded on a planar reference sample suggests [23,39].

Commercial graphite felts (Sigracet ECM 130, SGL Carbon) are used as cathode substrate. Prior the Pt deposition by ALD, the felts were thermally activated for 3 h at 450 °C (in air, muffle furnace, Nabertherm) [11,21]. The Pt catalyst was deposited on the activated graphite felts in a similar ALD

process as for the Ir and are described in detail in Refs. [11,21]. Pt was deposited in 30 cycles (nominal thickness on Si wafers of approx. 2 nm).

The Ir catalyst loading of the tubular anode PTE was determined by inductively coupled plasma optical emission spectrometry (ICP-OES). Three pieces of the Ir coated anode PTE (each about 1 cm long) were dissolved in 7 mL *aqua regia* following the procedure described in Ref. [22]. An Ir catalyst loading for 200 ALD cycles of 0.29 mg cm^{-2} was measured with a total error estimate of 0.03 mg cm^{-2}. A detailed description of the anodization and ALD catalyst coating process together with SEM pictures of such porous transport electrodes can be found in Ref. [23].

2.2.3. *Conductivity measurements*

Tubular porous titanium scaffolds were fabricated for conductivity measurements without the inner solid structure by AM. The length of the samples varied from 2 cm to 8 cm (approx. 8, 5, 3 and 2 cm), whereas both ends of the samples were polished ground flat. The conductivity was measured by a two point measurement with a device fabricated in-house while power and measurement cables were separately connected to copper contacts. The samples were pressed between two freshly polished Cu contacts by gravimetric force, applying a weight of 2.0 kg. An external current of 1.0 A was applied and the current and voltage drop over the entire sample was measured using multimeters Agilent 34410 A/34405 A. The measurements were repeated three times with three samples for every length while the same sample was removed and inserted again for each new measurement. The specific conductivity was determined by fitting a linear trend to the measured voltage drops. Length, inner and outer diameter were measured with a calliper with an accuracy of 0.05 mm.

The conductivity of the AM solid material was measured with AM flat bars of 0.5 mm thickness, 7 mm width and 32 mm length. The probes where pressed on two copper contacts with the distances of 7.5 mm, 10 mm, 15 mm, 20 mm. For the porous material a specific resistance of 22(2) mΩ mm and for the solid material a specific resistance of 4.2(1) mΩ mm has been determined.

2.3. *Electrochemical characterization*

For the electrochemical characterization a potentiostat SP150 in combination with a VMP3 Booster from Biologic was used in a two tank test rig as described in Ref. [21]. The cell is operated with 1 mol L^{-1} sulphuric acid in both half cells to achieve a sufficiently high protonic conductivity for the whole catalyst coated area. The flow rate was set to 2 mL $min^{-1}cm^{-2}$ with a peristaltic pump (Masterflex). All characterisations were performed at ambient pressure and at a temperature of 60 °C by using heat plates(CAT-m2021) and temperature sensors in the tanks, fluid cycles and the test cell housing.

The test routine consisted of a membrane break-in phase, a heat-up phase and the electrochemical characterization. During the membrane break in, a voltage of 1.6 V was applied for 2 h. The heat up took 2 h, while the temperature was nearly constant after 1 h. The techniques used for the electrochemical characterization were polarization curves (PC), electrochemical impedance spectroscopy (EIS) and chronoamperometry (CA) measurements. The cell voltage of all characterization methods was, except for 2 PCs, limited to 1.7 V in order to avoid degradation effects during characterizations. The PCs were recorded by a linear sweep voltammetry (LSV) with slope 20 mV min^{-1} from 1.2 V to 1.7 V. EIS measurements were performed to investigate the area specific cell resistance (ASR) and the activation resistances. EIS measurements were done in galvanostatic operation with average current density 15 mA cm^{-2} and a 1.5 mA cm^{-2} amplitude. A single PC was recorded by a linear voltage sweep with slope 20 mV min^{-1} from 1.2 V to 2.0 V to investigate the cell characteristics at high potentials. For the CA measurements, constant voltage was applied in 0.1 V steps from 1.2 V (theoretical OCV) to 1.7 V, holding each step for 2 h. At each voltage step, the mean value of the current over the last hour was determined for validating the PC data recorded with LSV. Another PC was recorded from 1.2 V to 2.0 V after the CA measurements to evaluate the voltage increase after 12 h of operation.

For one tubular cell, PCs were recorded from 0.1 mmol L^{-1} to 1000 mmol L^{-1} sulphuric acid as operating medium. Assuming complete dissociation the dilutions would correspond to pH values of 3.7, 2.7, 1.7, 0.7, −0.3 at 60 °C.

2.4. *Model description*

To define a tubular anode electrode design for the AM process which features a high electric conductivity in longitudinal direction and a high active area close to the membrane, the ohmic drop of three different PTE designs was analysed in FEM calculations (Comsol 5.6). The designs ‘tube’, ‘rods' and ‘cross' are shown in Fig. 3. All designs consist of a porous tube with extensions at both ends by solid tubes and fixed outer geometry: outer diameter (5 mm), length of the porous tube (102 mm) and length of the solid extensions at both sides (7 mm). In contrast to the ‘tube’ design, the designs ‘rods' and ‘cross' feature solid inner structures to increase the electrical conductivity. To balance the amount of titanium, the porous wall thickness for the ‘tube’ design is set to 1 mm and for the ‘cross' and ‘rods' to 0.75 mm, corresponding to the planar electrode thicknesses. The solid inner structure of ‘rods' and ‘cross' extends the porous tube by 2 mm at each side and form one solid part together with the extending tubes. In the design ‘rods', four rods with a diameter of 1 mm are placed equally spaced inside with a penetration depth of 0.25 mm into the porous tube. In the ‘cross’ design, the rods are connected with a 1 mm thick bar to the opposite rod.

To estimate the ASR contribution of the anode PTE designs, potential drops were calculated for a current source in the porous tubes connected at both end faces. The active electrode was limited to 100 mm of the porous tube.

The steady state model for the electric field E, current density J and potential ϕ is given by

$$\nabla \cdot J = Q_{j,v} \tag{1}$$

$$J = \sigma E \tag{2}$$

$$E = -\nabla \phi \tag{3}$$

and the additional assumptions.

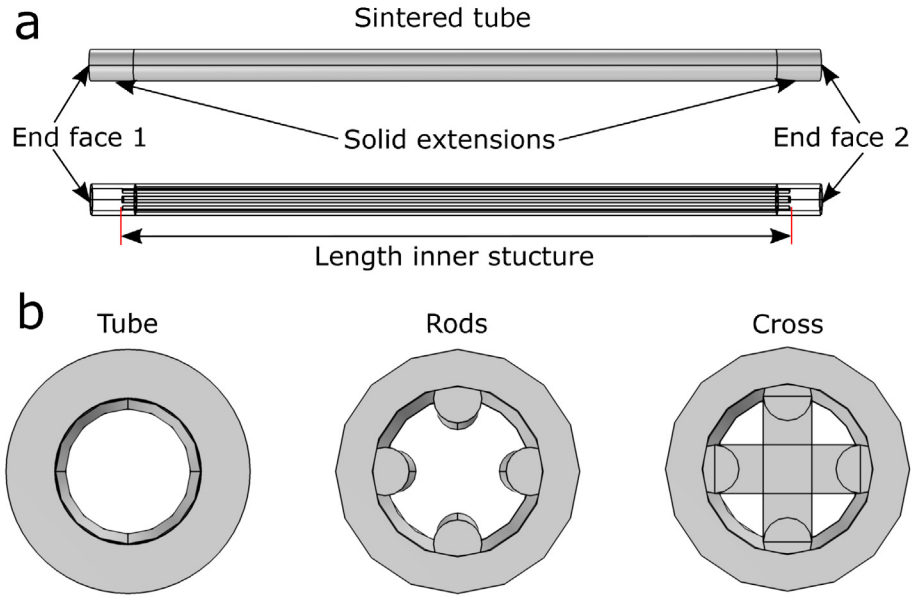

Fig. 3 – Anode PTE: (a) side view without and with visualization of inner structure, (c) front view of the three different designs.

- Homogeneous conductivities σ_p and σ_s of the porous and solid material that were determined experimentally described in section 2.2.
- Neglected contact resistances between the porous and solid material
- Homogeneous volume current source $Q_{j,v}$ over the active electrode

For the estimation of the ASR contribution of the anode PTE, a total current of 1 A was set for the homogeneous current source assuming homogeneous reaction rates in the PTE. Both end faces were set to ground and all other surfaces were electrically isolated. A conservative estimate of the ohmic resistance was calculated by using the maximum potential drop in the PTE and relating it to the current at one end face. The ASR is related to the projected active membrane area on the anode side, which is $\approx 15.71\,cm^2$.

To validate the model, the ohmic resistance of an external current in the anode PTE (end face 1 to end face 2) was calculated by applying a current of 1 A at one end face while the other end face was set to ground. All other surfaces were electrically isolated. The resistance was calculated form the potential drop between both end faces and the applied current. The simulation results were compared to measured resistances of the whole anode PTE using the tool described in section 2.2.

3. Results and discussion

3.1. *Planar cell performance*

The planar test cells described in Table 1 were characterized according to the measurement procedure of section 2.3 and demonstrated stable operation and leak tightness. Their performances were analysed by the LSV polarization curves shown in Fig. 4a using voltage limits 1.7 V and 2.0 V and additional EIS measurements.

We compare performance parameters in Table 2: At a cell potential of 1.7 V the Pl-1-1 and Pl-2-1 cells (100/200 cycles ALD and 1 mm electrode thickness) reached the highest current densities of 155–160 mA cm^{-2}, a value which is well below the

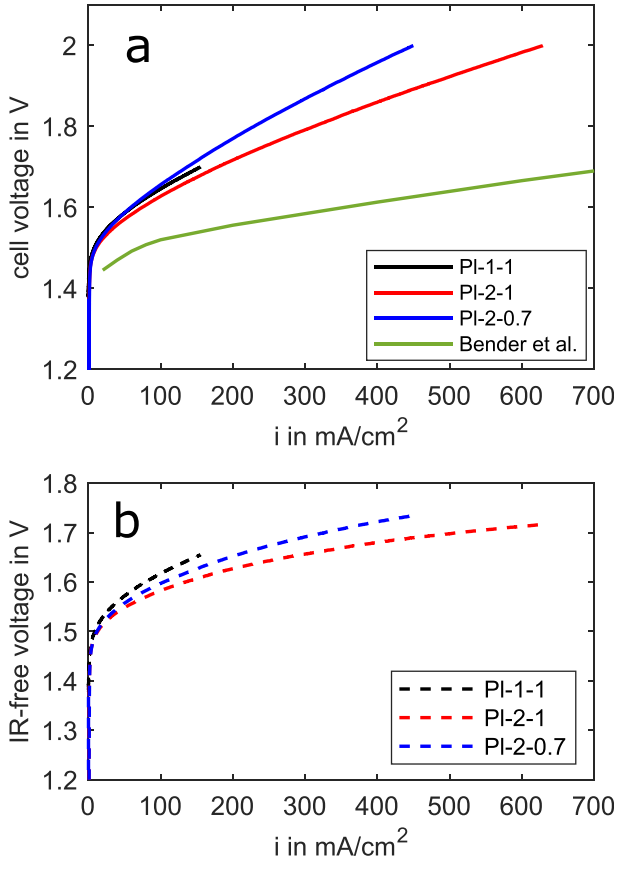

Fig. 4 – (a) Polarization curves of planar cells and a literature reference [40]; (b) IR-free polarization curves of planar cells.

Table 2 – Performance parameters of planar cells.

Cell-ID	Pl-1-1	Pl-2-0.7	Pl-2-1
$i_{1.7V}\,[mA/cm^2]$	155	125	160
$i_{2.0V}\,[mA/cm^2]$	–	450	630
$ASR_{EIS}\,[\Omega \cdot cm^2]$	0.30	0.60	0.45
$U_{IR-free@100mA/cm^2}\,[V]$	1.62	1.60	1.58
$U_{IR-free@400mA/cm^2}\,[V]$	–	1.72	1.68

value of the reference curve for a catalyst coated membrane (CCM) taken from the literature [40] but larger than the value for the Pl-2-0.7 cell. At 2.0 V the current densities increase to 450 – 630 mA cm^{-2}, the Pl-2-1 cell performing clearly better than Pl-2-0.7.

As the complete cell potentials reflects the contribution of the ohmic overpotential, we determined the ohmic resistances ASR_{EIS} displayed in Table 2 taken as the high frequency real axis intersections of the EIS Nyquist plots. Measured ASR values of the three cells are in the range 0.3 – 0.6Ωcm^{-2}, which is above typical literature values. The large span of the ASR is attributed to the variance of the cell assembly. For example cracks that sporadicly occurred in additively manufactured porous scaffolds could impact the electric conductivity, even though electrodes were inspected visually before the catalyst coating. A combination of a solid structure to conduct the electric current and a porous electrode, like in the tubular cell, reduces that risk.

To evaluate the impact of the catalyst coating and electrode thickness, the ohmic contribution was eliminated from the cell voltage. The IR-free cell voltage of the planar cells shown in Fig. 4b was obtained by subtracting the ohmic overpotential from the cell voltage using the ASR_{EIS}. The performance order of the cells changes for the IR-free cell voltage. The Pl-1-1 cell with 100 ALD cycles shows the highest residual overpotentials, while the cell with 200 cycles and 0.7 mm thickness gets closer to the cell with 200 cycles and 1 mm. In Table 2 the IR-free cell voltage is listed at 100 mA cm^{-2} and 400 mA cm^{-2} and exhibits only a small deviation for the two cells with 200 ALD cycles. In order to reduce the amount of precious metals, the electrode thickness 0.7 mm was chosen as a reference for the tubular AM electrode. We decided to use 200 cycle ALD cells in order to reduce ageing effects by applying a thicker catalyst layer.

3.2. *Model based tubular electrode design*

In order to reduce the ASR of the additively manufactured electrode, different electrode designs were simulated in the model described in section 2.4.

We validated the ASR model by comparing simulated electrical resistances to resistances measured with the device described in 2.2 for the design 'cross' and a constant current through the end faces. The calculated resistance of 57 mΩ is compatible with the experimentally measured 54(6) mΩ. Three scaffolds were measured with three repetitions while the scaffolds were inserted into the device for every measurement.

To estimate the ASR contribution of the anode PTE, the electric resistances of the three designs were now simulated with a volume current source in the porous tube and the electrical connections at both end faces. The resulting distributions of the current density are shown in Fig. 5 in two cross sections. In the 'tube' design, the current density grows homogeneously towards the end faces in the porous tube. In the designs 'rods' and 'cross', the current density concentrates as desired in the solid inner current conductor structure. It increases proportionally to the cross sectional area of the solid structure. Close to the transition from the porous to the solid tube, an elevated current in the porous tube of the rod design occurs as displayed in the cross sectional view parallel to the end face. Inhomogeneities in the porous material close to the transition interface would cause an increase of the cell resistance.

Simulated ASRs are 0.37Ωcm^{-2} for the tube design, 0.19Ωcm^{-2} for the rods design and 0.11Ωcm^{-2} for the cross design. The ASR of the membrane, the cathode PTE, and the outer current collector, which conduct just through plane, has

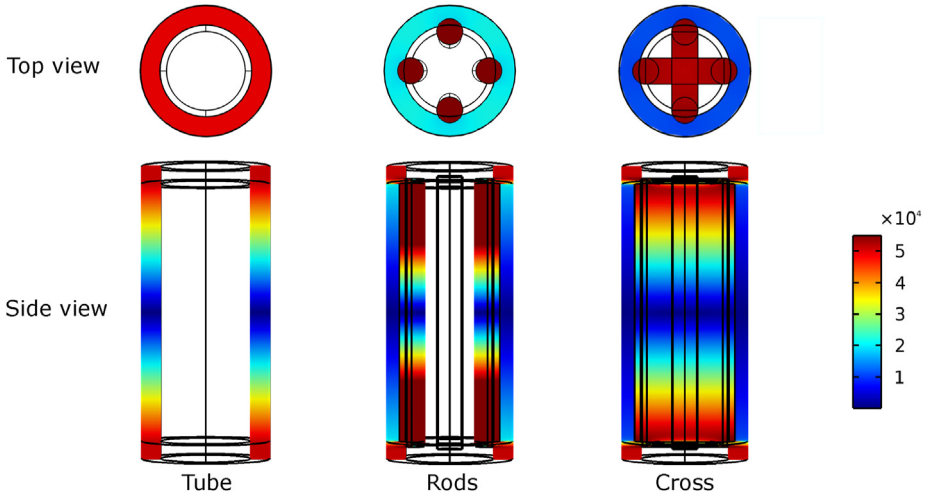

Fig. 5 – Current density distribution in the anode PTE scaffold designs: (top) - cross section parallel to end face 1 mm below the end of the porous tube; (bottom) - cross section perpendicular to end face through the inner structure.

been estimated to 0.11Ωcm^{-2}. For this estimate we used literature and data sheet values for the specific conductivities of 0.100 S cm for the extruded membrane [10], 42 S cm for an ECM 130 graphite felt and 5850 S cm for titanium grade 2. By this way a theoretical total cell ASR for the tubular cross design cell of 0.22Ωcm^{-2} has been estimated which is similar to literature values of planar cells with a CCM design [12,16,40]. The real cell ASR is expected to be higher since contact resistances and ionic conductivities have been neglected. Estimated ASR values of a tubular cell with 'tube' and 'rods' design are 0.47Ωcm^{-2} and 0.3Ωcm^{-2} and well above literature data.

One of the advantages of the tubular design is a decoupling of the cathodic and anodic current collector material, which enables a reduction of titanium. To compare the amount of titanium of the tubular and the commercial planar cell design, two assumptions were made for the tubular cell. First, the porous part of the tubular anodic titanium PTEs is neglected, as it is comparable to the porous transport layer of planar cells, in terms of porosity, thickness and amount of titanium. Second, the tubular outer cathodic current collector can be made of extruded graphite-polymer compounds and can be neglected. For the commercial planar cell design the amount of titanium is limited to the bipolar plates. Planar stacks are typically assembled with several cells connected in serial with thin bipolar plates between each cell and two thick end plates. As the number of cells stacked is usually high, the end plates can be neglected and the amount of titanium can be reduced to one bipolar plate per cell. In the literature, the thickness varies between 1 mm and 5 mm [41,42]. A. Mayyas et al. described typical cell dimensions of 680 mm^2 active area, 748 mm^2 active plus sealing area and 957 mm^2 bipolar plate area [42]. To consider theses variations in dimensions, a best and a worst case scenario was defined for the planar cell design. For the best case scenario, the bipolar plate area is defined as the active plus sealing area and 1 mm thickness and for the worst case scenario, the area is defined as the plate area and 5 mm thickness. The titanium mass related to the active area is 0.05 g cm^{-2}, 0.14 g cm^{-2} and 0.24 g cm^{-2} for the tubular tube, rods and cross design scenarios and is far below the values of 0.5 g cm^{-2} and 3.17 g cm^{-2} for the planar best and worst case scenarios. We thus concentrated on the 'cross' design for ASR reasons.

3.3. *Tubular cell performance*

Three tubular cells with AM anode in the 'cross' design were assembled and operated for 24 h according to the measurement routine. Even after additional storage of two cells for more than three months filled with 1 mol L^{-1} sulphuric acid no leakage of liquid or gas could be observed.

To evaluate the cell performance and reproducibility, we analysed polarization curves of three tubular cells and the corresponding planar cell 'Pl-2-07' shown in Fig. 6a. The cell voltages were measured by LSV at 60 °C and ambient pressure after the membrane heat up and break in phases. At 2.0 V the tubular cells reach a mean current density of 457 mA cm^{-2} with a standard error of 12 mA cm^{-2} which is well in line with the current density of the planar cell of 450 mA cm^{-2}. Compared to the previously published tubular

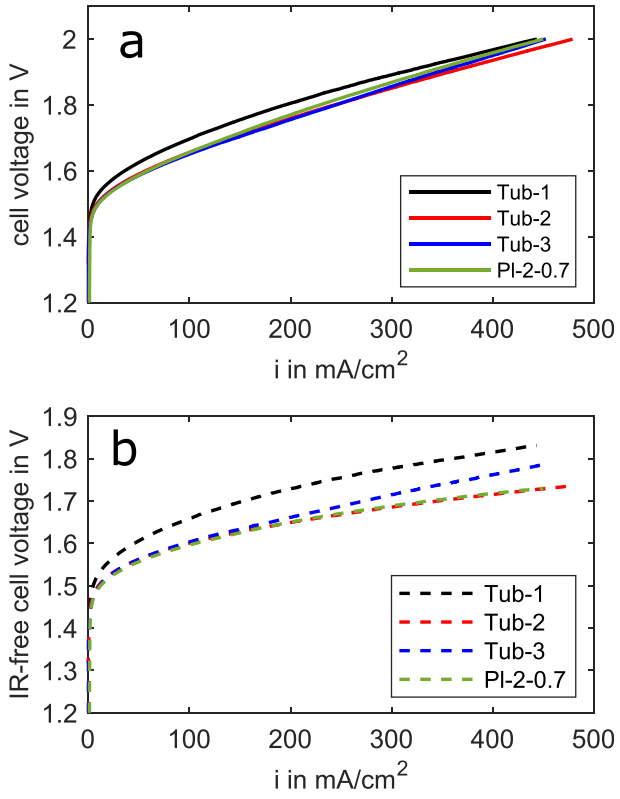

Fig. 6 – (a) Polarization curves and (b) IR-free polarization curves of the tubular and and the corresponding planar cells.

cell using a titanium felt based PTE [11], the current density is about three times higher. Published current densities of 2.0–2.5 A cm^{-2} at 2.0 V [12,40] for the typical CCM design are up to 5 times higher. However, the mass specific current density 1570Ag^{-1} of the tubular AM ALD cells related to the amount if iridium is much higher than typical values of 700 – 950Ag^{-1} for the commercial CCM design [40,43–45] (see Table 3). A stability study over 500 h with porous transport electrodes based on the same concept as in this study but different titanium substrates has shown a degradation rate of 67 μVh^{-1} which is higher than the rates of commercial PEM electrolysis cells with 2–10 μVh^{-1} [22]. However, these values can't be directly compared due to the current acidic environment in this feasibility study. A next step aims for adapting the electrode for replacing this harsh environment by water.

During the cell operation, a mean ASR over the three cells of 0.47 ± 0.05Ωcm^{-2} has been measured (see Table 3). In section 3.2 an ASR of 0.22Ωcm^{-2} has been estimated for this cell

Table 3 – Performance parameters of the tubular cells with the mean value and calculated error.

Cell ID	Tub-1	Tub-2	Tub-3	Mean	Error
$i_{2.0V}\,[mA/cm^2]$	440	480	450	457	12
$ASR\,[\Omega \cdot cm^2]$	0.38	0.55	0.47	0.47	0.05
$U_{IR-free@400mA/cm^2}\,[V]$	1.82	1.72	1.76	1.77	0.03
$i_{2.0V}\,[A/g]$	1520	1650	1550	1570	40

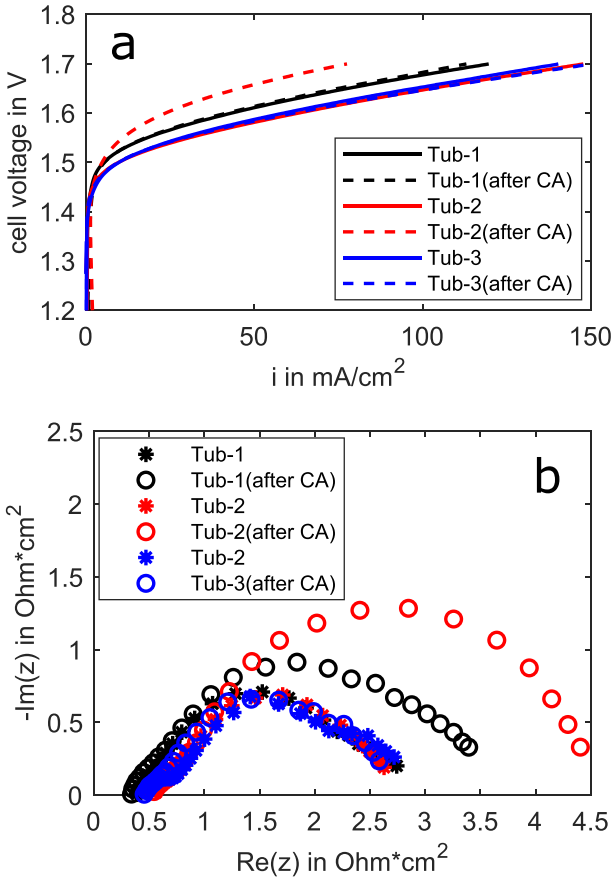

Fig. 7 – (a) Polarization curves and (b) Nyquist plots of tubular cells before and and after chronoamperometry measurements.

setup. We attribute the difference between estimated and measured ASR to additional contact resistances between the components and the additional ionic resistance in the sulphuric acid from the membrane surface to the electrode surface. Related to the previously published tubular cell with titanium felt based PTE, the measured ASR of the tubular AM anode cell is reduced by ≈50%. However further improvements are necessary to get closer to the typical ASR values for the CCM design of $\approx 0.2\Omega cm^{-2}$.

To eliminate the influence of the varying ASR, IR-free polarization curves were calculated as described for the planar cells and are shown in Fig. 6b. The IR-free polarization curve of the cells Tub-2, Tub-3 and Pl-2-0.7 cells are almost identical up to 200 mA cm^{-2}, which verifies the transfer of the electrode performance from the planar to the tubular design. At a fixed current density of 400 mA cm^{-2} the IR-free potential span a range from 1.7 V to 1.8 V. The main contribution to the difference is the shifted cell voltage of Tub-1 of 45 mV and the steeper incline of the IR-free cell voltage of Tub-3 above 200 mA cm^{-2}.

We evaluate the impact of the harsh environment during operation with 1 mol L^{-1} sulphuric acid on the tubular cell performance by considering the polarization curves and Nyquist plots of the EIS measurements before and after 12 h CA measurements as shown in Fig. 7. While the polarization curves of Tub-1 and Tub-3 are almost identical before and and after the CA measurements, the cell potential of Tub-2 increased. In the Nyquist plot of Tub-2, this increase is also visible in the second semicircle at frequencies <100 Hz. We attribute this increase to deteriorated reaction kinetics of the anode electrode due to ageing.

In order to evaluate the applicability of a cell including an extruded titanium free outer current collector we assembled a cell with an extruded outer current collector made of graphite-polypropylene-compound as shown in Fig. 8 on the right side. The platinum loading on the cathode side has been increased from 30 to 200 cycles, to reduce the cathodic contribution to the cell performance. An identical cell with a titanium current collector has been tested to identify the Outer current collector contribution. As shown in Fig. 8 the cell with the extruded outer current collector exhibits no losses in performance, even though a slightly higher ASR of $0.53\Omega cm^{-2}$ has been determined by EIS.

In contrast to the design of commercial planar PEM electrolysis cells, with a catalyst layer thickness of a few micrometers, the tubular porous transport electrode design features a catalyst distribution over the whole porous transport electrode thickness. 1 mol L^{-1} sulphuric acid was chosen as the

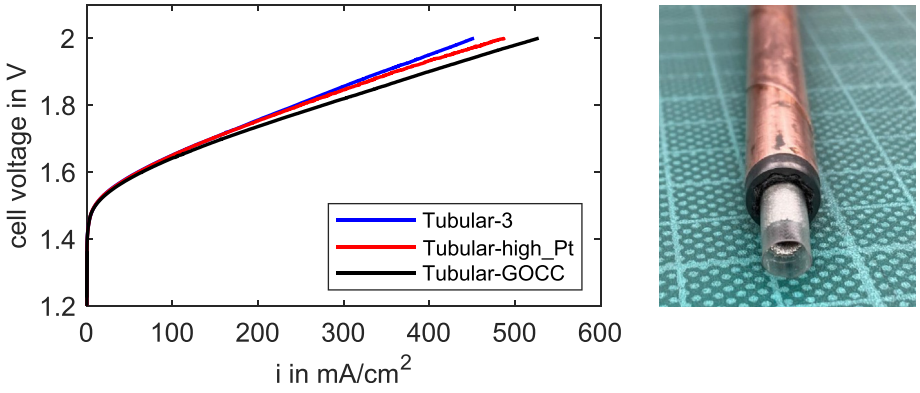

Fig. 8 – Left: Polarization curves of the tubular cell with a standard Platinum catalyst loading of (blue) a high loading (red) and a high loading plus a graphite outer current collector(GOCC) (black) right: photo of the assembled tubular cell with an extruded outer current collector. (For interpretation of the references to colour in this figure legend, the reader is referred to the Web version of this article.)

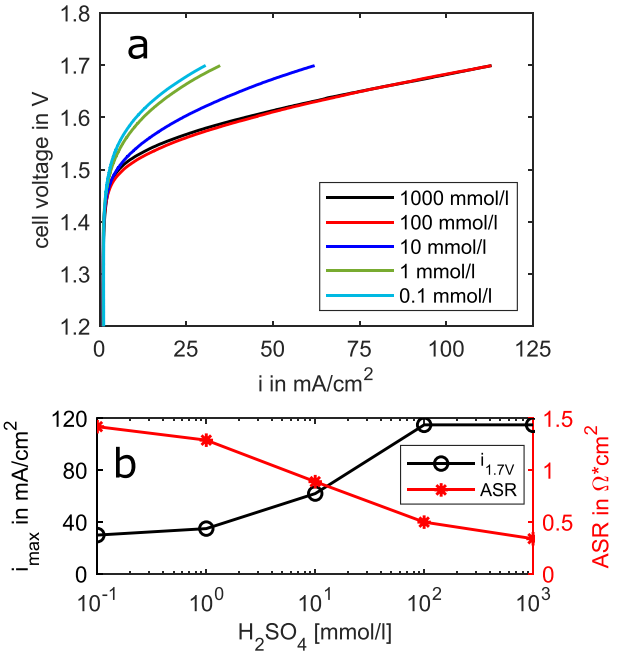

Fig. 9 – (a) Polarization curves and (b) current density at 1.7 V cell voltage and ASR of tubular cells in different sulphuric acid concentrations.

operating medium in both half cells to achieve a sufficiently high protonic conductivity for the whole catalyst coated area. As previously described, strong ageing effects could be observed during the operation. Beside to the cell components, all liquid facing system components such as reservoirs, pumps, piping etc. need to resist the acidic environment.

To reduce ageing effects we evaluated the cell operation in less harsh media. Polarization curves were recorded for one tubular cell at additional sulphuric acid concentrations from 0.1 to 100 mmol L^{-1} following the cell characterization after the chronoamperometric steps and are shown in Fig. 9a. While the cell performance remained nearly constant at a dilution of 100 mmol L^{-1} the cell performance decreased with decreasing sulphuric acid concentration. However, operating the cell at 100 mmol L^{-1} reduced the cell potentials for low current densities, even though the ASR was slightly increased, as shown in Fig. 9b. Thus, lower concentrations should be considered for long term stability measurements of this tubular PEM electrolysis cell within the PTE approach.

4. Conclusion

In this study, the feasibility of tubular PEMEL cells featuring extruded membranes, an extruded current collector and AM inner half cell electrodes has been demonstrated. A new cell design including a dedicated sealing concept especially for the potted tubular membrane has been developed and leak tight and stable cell operation has been achieved. The applicability of an extruded titanium free outer current collector leads to a drastic reduction of titanium needs compared to the commercial planar cell design.

In order to obtain high catalyst mass specific current densities a catalyst coating of the anode PTE by ALD combined with nanostructures by anodization has been applied. Starting from planar test cells the low catalyst loading of the AM electrodes has been optimized and successfully transferred to tubular cells.

Since the electrical contacts of the inner half cell are restricted to the cell ends, the ohmic resistance is a challenge for the tubular cell design. In order to lower the resistance, a model based design of the inner half cell combining AM porous titanium electrodes and AM titanium current conductors has been performed. The resulting experimental tubular cell ASR is a large reduction compared to a previously published first tubular cell with a titanium felt based PTE but still significantly larger than published ASRs for the typical CCM design. Further ASR improvements should concentrate on reducing contact resistances and ionic conduction path lengths in the PTE. The latter could be achieved by lowering the thickness of the active electrode parts. Selective PTE anodization on the membrane facing side could keep the active surface high and the precious metal loading low and a conventional membrane catalyst coating on the outer cathode half cell could be applied as well. To investigate the contribution of the components to the ASR and the cell potential, half cell potential measurements would be beneficial.

The experimental cell characterization exhibited current densities which are more than doubled compared to the previously published tubular cell with titanium felt PTE but still rather low compared to published current densities for the typical CCM design. However, due to the low iridium loading of 0.29 mg cm^{-2} for the anode PTE by applying ALD, a promising, very high mass specific current density of 1550 $A g^{-1}$ has been reached.

In this feasibility study the cells have been operated in 1 mol L^{-1} sulphuric acid in both half cells in order to achieve a high ionic conductivity. The harsh acidic environment is probably unfavorable for the cell stability since one tubular cell exhibited ageing effects. Extended degradation studies with different operating mediums and catalyst amounts are currently under investigation. Significantly lower acid concentrations than 0.1 mol L^{-1} led to decreasing performance. In the next development steps, a reduction of the PTE thickness and additional ionomer loading could allow for lower acidic concentrations or operation in water.

Though the tubular PEM electrolysis cell design still needs further improvements to compete with the established CCM design, it could already gain cost reduction benefits for applications with low current densities such as CO_2 reduction.

Acknowledgements

This work was performed within the research project Tubulyze and was supported by the German Federal Ministry of Education and Research (BMBF FKZ:03FS0564B). We thank Michael Jeske and Fumatech BWT GmbH for providing membrane material and the membrane conditioning and Rüdiger

Schweiss (SGL Carbon GmbH) for the supply with carbon fibre felt research samples.

Author contributions

• A. Laube: Conceptualization, cell design, cell modelling, cell assembly, conductivity and experimental, analysis of experimental results, writing, editing, review.

• B. Sánchez Batalla: ICP-OES and membrane measurements, corresponding writing in section 2, review.

• C. Weidlich: Validation, review, resources.

• S. ZallmannConceptualization, cell design, cell modelling: Fabrication of additively manufactured electrodes, corresponding writing in section 2, review.

• C. Körner: Validation, resources.

• A. Hofer: Anodization of scaffolds, ALD coating of electrodes, corresponding writing in section 2, review.

• J. Bachmann: Validation, review, resources.

• S. Fischer: Fabrication and quality management of extruded membranes, review.

• A. Chica: Supervision, validation, review, resources.

• T. Struckmann: Conceptualization, funding, supervision, editing, review, resources.

Declaration of competing interest

The authors declare that they have no known competing financial interests or personal relationships that could have appeared to influence the work reported in this paper.

REFERENCES

[1] Buttler A, Spliethoff H. Current status of water electrolysis for energy storage, grid balancing and sector coupling via power-to-gas and power-to-liquids: a review. Renew Sustain Energy Rev 2018;82:2440–54. https://doi.org/10.1016/j.rser.2017.09.003.

[2] Larscheid P, Lück L, Moser A. Potential of new business models for grid integrated water electrolysis. Renew Energy 2018;125:599–608. https://doi.org/10.1016/j.renene.2018.02.074.

[3] Pethaiah SS, Sadasivuni KK, Jayakumar A, Ponnamma D, Tiwary CS, Sasikumar G. Methanol electrolysis for hydrogen production using polymer electrolyte membrane: a mini-review. Energies 2020;13(22):5879. https://doi.org/10.3390/en13225879.

[4] Besserabov D. PEM electrolysis for hydrogen production. Apple Academic Press Inc.; 2015. URL, https://www.ebook.de/de/product/24366649/pem_electrolysis_for_hydrogen_production.html.

[5] Bertuccioli L, Chan A, Hart D, Lehner F, Madden B, Standen E. Study on developmentof water electrolysis in the eu. Tech. rep. 2014;(2):E4tech.

[6] Madheswaran DK, Jayakumar A. Recent advancements on non-platinum based catalyst electrode material for polymer electrolyte membrane fuel cells: a mini techno-economic review. Bull Mater Sci 2021;44(4):11. https://doi.org/10.1007/s12034-021-02572-6.

[7] Minke C, Suermann M, Bensmann B, Hanke-Rauschenbach R. Is iridium demand a potential bottleneck in the realization of large-scale PEM water electrolysis? Int J Hydrogen Energy 2021;46(46):23581–90. https://doi.org/10.1016/j.ijhydene.2021.04.174.

[8] Ressel S, Laube A, Fischer S, Chica A, Flower T, Struckmann T. Performance of a vanadium redox flow battery with tubular cell design. J Power Sources 2017;355:199–205. https://doi.org/10.1016/j.jpowsour.2017.04.066.

[9] Ressel S. Tubular all vanadium and vanadium/air redox flow cells. Ph.D. thesis, Universitat Politècnica de València; 2019.

[10] Ressel S, Kuhn P, Fischer S, Jeske M, Struckmann T. An all-extruded tubular vanadium redox flow cell - characterization and model-based evaluation. Journal of Power Sources Advances 2021;12:100077. https://doi.org/10.1016/j.powera.2021.100077.

[11] Laube A, Hofer A, Batalla BS, Ressel S, Chica A, Fischer S, Weidlich C, Bachmann J, Struckmann T. Tubular membrane electrode assembly for PEM electrolysis. Int J Hydrogen Energy 2022;47(36):15943–51. https://doi.org/10.1016/j.ijhydene.2022.03.135.

[12] Carmo M, Fritz DL, Mergel J, Stolten D. A comprehensive review on pem water electrolysis. Int J Hydrogen Energy 2013;38(12):4901–34. https://doi.org/10.1016/j.ijhydene.2013.01.151.

[13] Kumar SS, Himabindu V. Hydrogen production by PEM water electrolysis – a review. Materials Science for Energy Technologies 2019;2(3):442–54. https://doi.org/10.1016/j.mset.2019.03.002.

[14] Ayers K. The potential of proton exchange membrane–based electrolysis technology. Curr Opin Electrochem 2019;18:9–15. https://doi.org/10.1016/j.coelec.2019.08.008.

[15] Bernt M, Hartig-Weiß A, Tovini MF, El-Sayed HA, Schramm C, Schröter J, Gebauer C, Gasteiger HA. Current challenges in catalyst development for PEM water electrolyzers. Chem Ing Tech 2020;92(1–2):31–9. https://doi.org/10.1002/cite.201900101.

[16] Hegge F, Lombeck F, Ortiz EC, Bohn L, von Holst M, Kroschel M, Hübner J, Breitwieser M, Strasser P, Vierrath S. Efficient and stable low iridium loaded anodes for PEM water electrolysis made possible by nanofiber interlayers. ACS Appl Energy Mater 2020;3(9):8276–84. https://doi.org/10.1021/acsaem.0c00735.

[17] Yu H, Danilovic N, Wang Y, Willis W, Poozhikunnath A, Bonville L, Capuano C, Ayers K, Maric R. Nano-size IrOx catalyst of high activity and stability in PEM water electrolyzer with ultra-low iridium loading. Appl Catal B Environ 2018;239:133–46. https://doi.org/10.1016/j.apcatb.2018.07.064.

[18] Ayers KE, Renner JN, Danilovic N, Wang JX, Zhang Y, Maric R, Yu H. Pathways to ultra-low platinum group metal catalyst loading in proton exchange membrane electrolyzers. Catal Today 2016;262:121–32. https://doi.org/10.1016/j.cattod.2015.10.019.

[19] Kúš P, Ostroverkh A, Ševčíková K, Khalakhan I, Fiala R, Skála T, Tsud N, Matolin V. Magnetron sputtered ir thin film on TiC-based support sublayer as low-loading anode catalyst for proton exchange membrane water electrolysis. Int J Hydrogen Energy 2016;41(34):15124–32. https://doi.org/10.1016/j.ijhydene.2016.06.248.

[20] Hrbek T, Kúš P, Yakovlev Y, Nováková J, Lobko Y, Khalakhan I, Matolín V, Matolínová I. Sputter-etching treatment of proton-exchange membranes: completely dry thin-film approach to low-loading catalyst-coated membranes for water electrolysis. Int J Hydrogen Energy 2020;45(41):20776–86. https://doi.org/10.1016/j.ijhydene.2020.05.245.

[21] Laube A, Hofer A, Ressel S, Chica A, Bachmann J, Struckmann T. PEM water electrolysis cells with catalyst coating by atomic layer deposition. 2021. https://doi.org/10.1016/j.ijhydene.2021.09.153.
[22] Batalla BS, Laube A, Hofer A, Struckmann T, Bachmann J, Weidlich C. Degradation studies of proton exchange membrane water electrolysis cells with low platinum group metals – catalyst coating achieved by atomic layer deposition. Int J Hydrogen Energy 2022;47(94):39719–30. https://doi.org/10.1016/j.ijhydene.2022.09.159.
[23] Hofer A, Wachter S, Döhler D, Laube A, Batalla BS, Fu Z, Weidlich C, Struckmann T, Körner C, Bachmann J. Practically applicable water oxidation electrodes from 3d-printed ti6al4v scaffolds with surface nanostructuration and iridium catalyst coating. Electrochim Acta 2022;417:140308. https://doi.org/10.1016/j.electacta.2022.140308.
[24] Arenas L, de León CP, Walsh F. 3d-printed porous electrodes for advanced electrochemical flow reactors: a ni/stainless steel electrode and its mass transport characteristics. Electrochem Commun 2017;77:133–7. https://doi.org/10.1016/j.elecom.2017.03.009.
[25] Browne MP, Novotný F, Sofer Z, Pumera M. 3d printed graphene electrodes' electrochemical activation. ACS Appl Mater Interfaces 2018;10(46):40294–301. https://doi.org/10.1021/acsami.8b14701.
[26] Ambrosi A, Moo JGS, Pumera M. Helical 3d-printed metal electrodes as custom-shaped 3d platform for electrochemical devices. Adv Funct Mater 2015;26(5):698–703. https://doi.org/10.1002/adfm.201503902.
[27] Ambrosi A, Pumera M. Self-contained polymer/metal 3d printed electrochemical platform for tailored water splitting. Adv Funct Mater 2017;28(27):1700655. https://doi.org/10.1002/adfm.201700655.
[28] Ambrosi A, Pumera M. Multimaterial 3d-printed water electrolyzer with earth-abundant electrodeposited catalysts. ACS Sustainable Chem Eng 2018;6(12):16968–75. https://doi.org/10.1021/acssuschemeng.8b04327.
[29] Bui JC, Davis JT, Esposito DV. 3d-printed electrodes for membraneless water electrolysis. Sustain Energy Fuels 2020;4(1):213–25. https://doi.org/10.1039/c9se00710e.
[30] Agudelo MCB, Hampe M, Reiber T, Abele E. Investigation of porous metal-based 3d-printed anode GDLs for tubular high temperature proton exchange membrane fuel cells. Materials 2020;13(9):2096. https://doi.org/10.3390/ma13092096.
[31] Yang G, Yu S, Mo J, Kang Z, Dohrmann Y, List FA, Green JB, Babu SS, Zhang F-Y. Bipolar plate development with additive manufacturing and protective coating for durable and high-efficiency hydrogen production. J Power Sources 2018;396:590–8. https://doi.org/10.1016/j.jpowsour.2018.06.078.
[32] Yang G, Mo J, Kang Z, Dohrmann Y, List FA, Green JB, Babu SS, Zhang F-Y. Fully printed and integrated electrolyzer cells with additive manufacturing for high-efficiency water splitting. Appl Energy 2018;215:202–10. https://doi.org/10.1016/j.apenergy.2018.02.001.
[33] Yang G, Xie Z, Yu S, Li K, Li Y, Ding L, Wang W, Zhang F-Y. All-in-one bipolar electrode: a new concept for compact and efficient water electrolyzers. Nano Energy 2021;90:106551. https://doi.org/10.1016/j.nanoen.2021.106551.
[34] Chisholm G, Kitson PJ, Kirkaldy ND, Bloor LG, Cronin L. 3d printed flow plates for the electrolysis of water: an economic and adaptable approach to device manufacture. Energy Environ Sci 2014;7(9):3026–32. https://doi.org/10.1039/c4ee01426j.
[35] Yang G, Yu S, Kang Z, Dohrmann Y, Bender G, Pivovar BS, Green JB, Retterer ST, Cullen DA, Zhang F-Y. A novel PEMEC with 3d printed non-conductive bipolar plate for low-cost hydrogen production from water electrolysis. Energy Convers Manag 2019;182:108–16. https://doi.org/10.1016/j.enconman.2018.12.046.
[36] Schlicht S, Büttner P, Bachmann J. Highly active ir/TiO2 electrodes for the oxygen evolution reaction using atomic layer deposition on ordered porous substrates. ACS Appl Energy Mater 2019;2(3):2344–9. https://doi.org/10.1021/acsaem.9b00402.
[37] Körner C. Additive manufacturing of metallic components by selective electron beam melting — a review. Int Mater Rev 2016;61(5):361–77. https://doi.org/10.1080/09506608.2016.1176289.
[38] Fu Z, Körner C. Actual state-of-the-art of electron beam powder bed fusion. European Journal of Materials 2022;2(1):54–116. https://doi.org/10.1080/26889277.2022.2040342.
[39] Hofer A, Bochmann S, Bachmann J. Properties, performance and stability of iridium-coated water oxidation electrodes based on anodized titanium felts. Sustain Energy Fuels 2021;5(2):478–85. https://doi.org/10.1039/d0se01577f.
[40] Bender G, Carmo M, Smolinka T, Gago A, Danilovic N, Mueller M, Ganci F, Fallisch A, Lettenmeier P, Friedrich K, Ayers K, Pivovar B, Mergel J, Stolten D. Initial approaches in benchmarking and round robin testing for proton exchange membrane water electrolyzers. Int J Hydrogen Energy 2019;44(18):9174–87. https://doi.org/10.1016/j.ijhydene.2019.02.074.
[41] Holst M, Aschbrenner S, Smolinka T, Voglstätter C, Grimm G. Cost forecast for low-temperature electrolysis – technology driven bottom-up prognosis for pem and alkaline water electrolysis systems. Tech. rep., Fraunhofer Institute for Solar Energy Systems ISE; 2021.
[42] Mayyas A, Ruth M, Pivovar B, Bender G, Wipke K. Manufacturing cost analysis for proton exchange membrane water electrolyzers. Golden: Tech. rep., National Renewable Energy Laboratory; 2019. NREL/TP-6A20-72740. URL, https://www.nrel.gov/docs/fy10osti/72740.pdf.
[43] Bromberger K, Ghinaiya J, Lickert T, Fallisch A, Smolinka T. Hydraulic ex situ through-plane characterization of porous transport layers in PEM water electrolysis cells. Int J Hydrogen Energy 2018;43(5):2556–69. https://doi.org/10.1016/j.ijhydene.2017.12.042.
[44] Parra-Restrepo J, Bligny R, Dillet J, Didierjean S, Stemmelen D, Moyne C, Degiovanni A, Maranzana G. Influence of the porous transport layer properties on the mass and charge transfer in a segmented PEM electrolyzer. Int J Hydrogen Energy 2020;45(15):8094–106. https://doi.org/10.1016/j.ijhydene.2020.01.100.
[45] Kang Z, Alia SM, Young JL, Bender G. Effects of various parameters of different porous transport layers in proton exchange membrane water electrolysis. Electrochim Acta 2020;354:136641. https://doi.org/10.1016/j.electacta.2020.136641.